International Journal of Nanomedicine

Dovepress

open access to scientific and medical research

Open Access Full Text Article

ORIGINAL RESEARCH

pH-Responsive Nanoparticles for Enhanced Antitumor Activity by High-Intensity Focused Ultrasound Therapy Combined with Sonodynamic Therapy

Hui Gao[1,2,*]
Zhaoxia Wang[1,2,*]
Mixiao Tan[1]
Weiwei Liu[1]
Liang Zhang[1]
Ju Huang[1]
Yang Cao[1]
Pan Li[1]
Zhigang Wang[1]
Jiexin Wen[2]
Tingting Shang[1]
Haitao Ran[1]

[1]Chongqing Key Laboratory of Ultrasound Molecular Imaging & Institute of Ultrasound Imaging, The Second Affiliated Hospital of Chongqing Medical University, Chongqing, People's Republic of China; [2]Department of Ultrasound, Children's Hospital of Chongqing Medical University, Chongqing, People's Republic of China

*These authors contributed equally to this work

Background: Therapeutic ultrasound (US) has been extensively explored for its inherent high tissue-penetrating capability and on-demand irradiation without radioactive damage. Although high-intensity focused ultrasound (HIFU) is evolved as such an outstanding US-based approach, its insufficient therapeutic effect and the high-intensity induced potential damage to surrounding normal tissues hindered its development towards practical application. As opposed to high intensity ultrasound, sonodynamic therapy (SDT) is a low intensity US-based method which exhibits certain therapeutic effects against cancer via sonosensitizers-generated reactive oxygen species (ROS) overproduction.

Methods: Hematoporphyrin monomethyl ether (HMME) loaded $CaCO_3$ nanoparticles (designated as Ca@H) were synthesized by a gas diffusion method. The pH-responsive performance, in vitro SDT, ex vivo HIFU therapy (HIFUT), photoacoustic (PA) imaging and in vivo HIFUT combined with SDT were investigated thoroughly.

Results: Ca@H NPs gradually decomposed in acid tumor microenvironment, produced CO_2 and released HMME. Both CO_2 and HMME enhanced photoacoustic (PA) imaging. The generated CO_2 bubbles also enhanced HIFUT by inducing an enlarged ablation area. The tumor ablation efficiency (61.04%) was significantly improved with a combination of HIFU therapy and SDT.

Conclusion: pH-responsive Ca@H NPs have been successfully constructed for PA imaging-guided/monitored HIFUT combined with SDT. With the assistance of pH-responsive Ca@H NPs, the combination of these two US-based therapies is expected to play a role in the treatment of non-invasive tumor in the future.

Keywords: ultrasound, high-intensity focused ultrasound therapy, sonodynamic therapy, $CaCO_3$ nanoparticles, nanomedicine

Introduction

From imaging to therapeutics, the versatility of ultrasound (US) has received increased attention in recent years.[1–4] Due to the low cost-effectiveness, absence of ionizing radiation and deep-tissue imaging depth, US imaging is the most common clinical diagnosis method.[5,6] In particular, with the inherent high tissue-penetrating capability and on-demand irradiation without radioactive damage, US has also been developed into various therapeutic modalities.[7,8] Among these US-based techniques, microwave therapy, high-intensity focused ultrasound (HIFU)

Correspondence: Haitao Ran
Chongqing Key Laboratory of Ultrasound Molecular Imaging & Institute of Ultrasound Imaging, The Second Affiliated Hospital of Chongqing Medical University, No. 76 Linjiang Road, Yuzhong District, Chongqing, 400010, People's Republic of China
Tel +86-13-512373563
Email ranhaitao@cqmu.edu.cn

Received: 2 September 2021
Accepted: 24 December 2021
Published: 25 January 2022

therapy (HIFUT), sonodynamic therapy (SDT), etc., have been extensively explored for their inimitable advantages.[9–11] For instance, as a promising non-invasive cancer treatment method, HIFU ablation developed rapidly in the clinical treatment against solid tumors (eg, breast cancer, cervical carcinoma) due to its excelled thermal and mechanical effects.[12–15] Its effectiveness and feasibility are unparalleled by traditional surgery, chemotherapy and radiotherapy. However, its disadvantages, such as decreased treatment efficiency with increasing depth, and reduced HIFU acoustic power with rapid blood flow, usually lead to the persistence of residual tumor cells.[16]

It is also concerning that although increasing the operating energy of HIFU seems to achieve some enhancement, the overwhelmed acoustic intensity can impair normal tissue and cause adverse side effects, such as nerve injury, transient pain, and skin burns.[17,18] Therefore, it is challenging to acquire high therapeutic efficiency with controlled therapeutic power in HIFUT. Previously, some studies have successfully used gas-loaded microbubbles to enhance HIFU cancer surgery through gas-dependent cavitation.[19] However, oversized (a few microns in diameter) bubbles led to a relatively shorter circulation time and limited its clinical transformation. Calcium carbonate ($CaCO_3$) nanoparticles (NPs) have excellent biocompatibility and biodegradability, which brings new opportunities for cancer theranostics. $CaCO_3$ is mostly stable under neutral pH and may decompose to release CO_2 when interact with acidity.[20,21] The pH-responsiveness enables nano-scaled $CaCO_3$ to become an ideal drug delivery system as well as a theranostic platform responding to tumor microenvironment.[20,22–24] By virtue of the principle of enhancing HIFU by gas-dependent cavitation, $CaCO_3$ also shows potential for HIFU enhancement due to its CO_2 generation capability.

Although promising, it is difficult to ablate lesions bordering normal tissues with HIFU, because the US energy used for HIFU is relatively high and it is easy to damage the surrounding normal tissues. To minimize the damage to adjacent tissue, while the primary solid tumor has been ablated, SDT is introduced to remove the remnant lesion. As a thriving approach with well-established therapeutic performances, SDT relies on sonosensitizer-mediated reactive oxygen species (ROS) overproduction.[9,25] Compared to HIFUT, SDT only applies moderate energy. It is a desirable complementary modality with HIFUT. Different from HIFUT with high-intensity short duration pulse US, US used in SDT is moderate-intensity long sustaining wave, which will not cause damage to normal tissues without existence of sonosensitizers.

Herein, to obtain the maximum therapeutic effect of HIFUT and prevent tumor recurrence, typical sonosensitizer-hematoporphyrin monomethyl ether (HMME) was loaded in the $CaCO_3$ (designated as Ca@H) for combined HIFUT and SDT. As illustrated in Scheme 1, after intravenous injection, these Ca@H nanoparticles (NPs) can accumulate in tumor site by the typical enhanced permeability and retention (EPR) effect during blood circulation. Ca@H NPs would gradually decompose in the mildly acidic tumor microenvironment, producing CO_2 and releasing HMME. Both CO_2 and HMME enhance photoacoustic (PA) imaging, providing US-based therapeutic guidance and monitoring.[26–29] Upon high-intensity short duration pulse US explosion, the generated CO_2 bubbles lead to a cavitation effect and strengthens HIFUT by inducing enlarged ablation area. Then, moderate-intensity long-sustaining US will be employed for SDT to treat the residual lesions. Therapeutic performances, as well as PA imaging capability, were assessed both in vitro and in vivo. This study explored and rationally organized different US-based modalities for optimized cancer theranostic. The hierarchical arrangements for HIFUT, SDT, and PA imaging established an innovative strategy that accurately eliminates tumor tissue with minimum adverse effects.

Materials and Methods

Materials

Ethanol (anhydrous, >99.7) and chloroform were obtained from Chongqing Chuandong Chemical Co. Ltd. (Chongqing, China). Calcium chloride dihydrate ($CaCl_2 \cdot 2H_2O$), ammonium bicarbonate (NH_4HCO_3) and 1.3-diphenylisobenzofuran (DPBF) were purchased from Sigma Aldrich (MO, USA). HMME was purchased from Shanghai D&B Biotechnology Co., Ltd. (Shanghai, China). Nuclear dye 4′,6-Diamidino-2-phenylindole (DAPI) was purchased from Beyotime Biotechnology (Shanghai, China). Cell Counting Kit-8 (CCK-8) was bought from MedChemExpress (New Jersey, USA). Calcein-AM (CAM) and propidium iodide (PI) were obtained from Dojindo (Japan). Proliferating cell nuclear antigen (PCNA) antibody was obtained from Servicebio Technology Co., Ltd (Wuhan, China). Singlet oxygen sensor green (SOSG) was purchased from Thermo Fisher

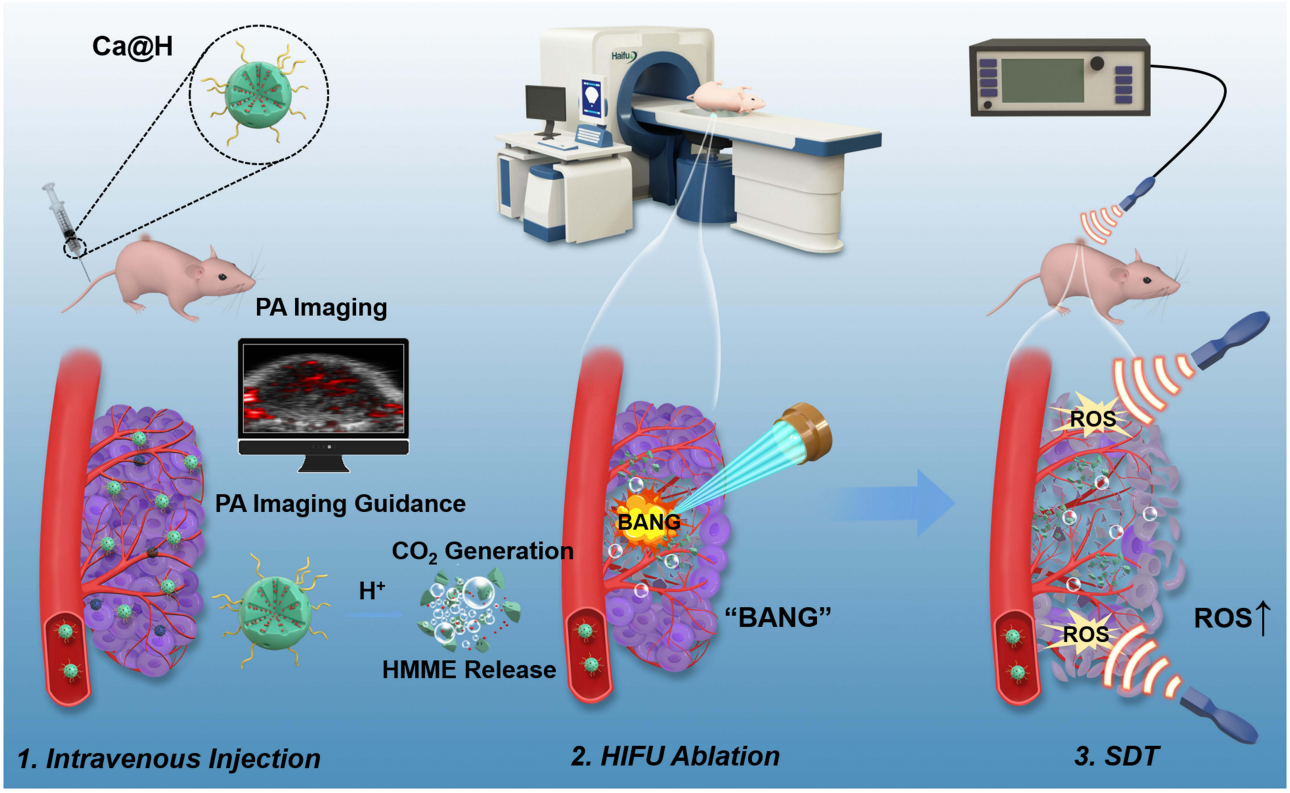

Scheme 1 Schematic illustration of pH-responsive Ca@H NPs-mediated tumor theranostics including i) CO_2 generation, HMME release in the acidic tumor microenvironment, ii) CO_2/HMME-enhanced PA imaging, iii) CO_2 bubbles-enhanced HIFUT, and iv) HMME-mediated SDT for the residual lesions.

Scientific (California, USA). 1.2-dioleoyl-sn-glycerol -3-phosphate (sodium salt) (DOPA) was purchased from Avanti Polar Lipids, Inc. (Alabaster, Alabama, USA).1,2-distearoyl-sn-glycero-3-phosphoethanolamine-N-[methoxy(polyethylene glycol)-2000 (DSPE-PEG2000), 1.2-dipalmitoyl-sn-glycero-3-phospha-tidylcholine (DPPC) and cholesterol were synthesized by Xi'an Ruixi Biological Technology Co., Ltd (Xi'an, China).

Synthesis of Ca@H NPs

Ca@H NPs were prepared by a gas diffusion method. In detail, 150 mg of $CaCl_2$ and 10 mg of HMME were dissolved in 100 mL ethanol in a beaker covered by an aluminum foil with punctured several pores. Subsequently, the above solution was maintained in a vacuum drying chamber containing 5 g dry NH_4HCO_3. After 48 h, Ca@H NPs were collected by centrifugation at 10,000 xg for 5 min and rinsed three times with anhydrous ethanol. Ca@H NPs (20 mg) in 5 mL ethanol solution and 1 mL DOPA solution (4 mg/mL in chloroform) were mixed under ultrasonication (20 min, in ice bath). The resulting turbidity solution was centrifuged to remove excess DOPA and then re-dispersed in 2 mL chloroform. DPPC (8 mg), cholesterol (4 mg), and DSPE-PEG-2000 (16 mg) were mixed with the above sediments and stirred overnight. Chloroform is removed by a rotary evaporation method, and Ca@H NPs with good dispersibility were obtained.

Characterization of Ca@H

The morphology of Ca@H was visualized by SEM (Hitachi SU8020, Japan) and TEM (JEM-1200, JEOL, Japan). The average hydrodynamic diameter and surface zeta potential of Ca@H NPs were measured by a Malvern Nanozetasizer (Nano ZS90, Malvern Panalytical, UK). And the UV-Vis spectra of HMME samples (0.5, 1.0, 2.0, 3.0, 4.0, 5.0 and 6.0 μg/mL) were collected using a SpectraMax Paradigm Multi-Mode Microplate Reader (Molecular Devices, Silicon Valley, USA). The loading efficiency of HMME was calculated by the following equation.

Loading efficiency = (weight of HMME input – unloaded HMME)/weight of HMME input

pH-Responsive Performance and in vitro ROS Generation

The morphology change of Ca@H NPs in mild acidity was observed by TEM. Buffer solutions of pH = 5.5 and 6.5 were

prepared. Ca@H NPs were added to the buffer. The mixture was subjected to magnetic stirring (120 rpm). TEM specimens were prepared after 2 h of stirring. The HMME release performance was determined by placing Ca@H NPs in buffers with pH at 5.5, 6.5, and 7.4, respectively. After applying magnetic stirring (120 rpm) for a certain time (0, 10, 30, 60, and 120 min). An aliquot of 2 mL was withdrawn for a centrifugation process to collect the supernatant. The released HMME amount/percentage was determined by the Spectra Max Paradigm Multi-Mode Microplate Reader. Different concentrations of Ca@H NPs (2 mg/mL, 6 mg/mL, 10 mg/mL) were dispersed in buffers at different pH (7.4, 6.5 and 5.5). The mixtures were placed in glass vials sealed with rubber stoppers and connected to an air quality meter (IAQ-7515, TSI Inc., Shoreview, MN, USA). After stirring for 24 hours, the CO_2 percentages in the output were measured and recorded. After 2 h of stirring in buffers at pH = 7.4, 6.5 or 5.5, these suspensions (the corresponding HMME concentration was 10 μg/mL) containing SOSG (15 μg/mL) was irradiated by US (1.5 W/cm^2) for different time (15, 30, 60 and 90 s), and changes in fluorescence intensities were measured using a microplate reader. The singlet oxygen yield of Ca@H NPs was measured by monitoring the dye-sensitized photooxidation of DPBF. Typically, DPBF was dissolved in DMSO at a concentration of 100 μM. In order to simulate the release of HMME of Ca@H NPs in the acidic tumor microenvironment, Ca@H NPs were dispersed in buffer of pH = 6.0 (the corresponding HMME concentration was 20 μg/mL), then the mixture was subjected to magnetic stirring (120 rpm, 2 h). Minimum DMSO was used to dissolve HMME and PBS was used to adjust the concentration to 20 μg/mL. Next, Ca@H suspension (1.5 mL) or HMME (1.5 mL) was mixed DPBF (1.5 mL) and exposed to US irradiation at 1.5 W/cm^2 for 0, 15, 30, 60, 90, 120 and 180 s, respectively. The absorbance of the mixture was then measured at λ = 410 nm. The singlet oxygen yield of Ca@H NPs ($\Phi(^1O_2)^{Ca@H}$) was calculated by plotting -Ln ([DPBF]/[DPBF]$_0$) against the irradiation time and followed by the equation as follows.[30–32]

$$\Phi(^1O_2)^{Ca@H} = \Phi(^1O_2)^{HMME} \times (K^{Ca@H}/ K^{HMME})$$

Where HMME was used as a reference ($\Phi(^1O_2)^{HMME} = 0.5$),[33] $K^{Ca@H}$ and K^{HMME} refer to the corresponding slopes of the plots, respectively.

Intracellular Uptake of Ca@H

Murine breast cancer cells (4T1) were purchased from Shanghai Zhong Qiao Xin Zhou Biotechnology Co., Ltd. (Shanghai, China) and maintained in Roswell Park Memorial Institute (RPMI) 1640 medium (Gibco) containing 1% penicillin-streptomycin (Beyotime Biotechnology) and 10% fetal bovine serum (Shanghai Zhong Qiao Xin Zhou Biotechnology Co., Ltd.). To observe the intracellular uptake of Ca@H NPs, 4T1 cells were seeded in CLSM-specific dishes at a concentration of 1×10^5 per dish. After 24 h, cells were co-incubated with Ca@H NPs (equivalent concentration of HMME was 30 μg/mL) for 4 h. At predetermined time intervals (2 h and 4 h), the cells were rinsed with PBS and fixed with 4% paraformaldehyde. After being stained by DAPI, cells were observed by CLSM. To further characterize the endocytosis efficacy of Ca@H NPs, flow cytometry was carried out. Cells were prepared similarly as for CLSM observations except that cells were directly trypsinized after co-incubation with Ca@H NPs.

Intracellular ROS Generation

Similarly, 1×10^5 4T1 cells were seeded into CLSM-specific dishes or 12-well plates and incubated for 24 h. Then the cells were co-incubated with Ca@H NPs suspensions (equivalent concentration of HMME was 30 μg/mL) at pH 6.0 or 7.4 for 4 h and then stained with and DCFH-DA (30 μM). After that, cells were subjected to US irradiation (1.5 W/cm^2) for 90s and observed by CLSM. Fluorescent intensities within three microscopic fields for each group were quantified using Image J software. Flow cytometry was carried out to quantitatively analyze ROS generation.

In vitro Cytotoxic of Ca@H Combined with US Irradiation

4T1 cells (1×10^4) were seeded in 96-well plates and cultured overnight. Then the medium in the plate was replaced with fresh medium containing various concentrations of Ca@H NPs. After 4 h, 12 h and 24 h incubation, a standard CCK-8 kit was used to test the cell viabilities. To test the in vitro SDT efficiency, as a comparison, cells without US irradiation were set as the control group. Besides, cells in plates were randomly divided into five groups including: control, US, Ca@H, Ca@H + US (pH = 7.4) and Ca@H + US (pH = 6.0). When the cells reached 80–90% confluency, the above treatments were performed. The cells in the corresponding US groups were irradiated by US for 90 s at 1.5 W/cm.^{2}The absorbance of the wells were measured using a plate reader and the cell viability was calculated. Meanwhile, the cells were co-stained with CAM/PI to

distinguish the live and dead cells under CLSM. In addition, the cell damage rates were detected by flow cytometry.

Animal Model

In our experiments, specific-pathogen-free BALB/c nude mice were purchased from Chongqing Medical University. All animal experiments were performed in the Chongqing Medical University Laboratory Animal Center followed by the Association for Assessment and Accreditation of Laboratory Animal Care guidelines and approved by Ethics Committee of the Second Affiliated Hospital of Chongqing Medical University. To establish the transplant tumor models, 4T1 cells suspended in PBS (1×10^6 cells/100μL) were subcutaneously injected into the flank of the mice for a standard incubation.

Ex vivo HIFU Ablation

All HIFU-associated experiments were conducted on Model-JC200 Focused Ultrasound Tumor Therapeutic System (Chongqing Haifu Medical Technology Co., Ltd., Chongqing, China). Fresh bovine liver tissues were employed to assess the enhanced HIFU ablation. The bovine liver tissues were degassed. Ca@H NPs in PBS (50 μg/mL, 200 μL) were directly injected into bovine liver tissues and the injection sites were observed by a diagnostic US unit. Immediately, HIFU ablation (120 W, 5 s) was conducted on the injection regions. Then, the digital photos of ablated-bovine liver tissues were collected, and the ablation areas were measured. Meanwhile, H&E staining was carried out to observe the cell state. In addition, Ca@H NPs in different pH were assessed to compare the HIFU ablation efficiency. Ultrastructural analysis of liver tissues after different treatments were further carried out by TEM after fixation with glutaraldehyde.

PA Imaging Enhancement Assisted by Ca@H

To evaluate the PA imaging performance of Ca@H NPs, the Ca@H NPs suspension was scanned by PA laser with excitation wavelength ranging from 680 nm to 970 nm to pinpoint the optimal excitation wavelength for imaging. Afterward, $CaCO_3$ or Ca@H NPs dispersed in water at pH 5.5, 6.5, and 7.4 were added in the agar gel model. The corresponding PA images were acquired, and the PA signal intensities were measured. To further investigate in vivo PA imaging performance, 4T1 xenograft tumors were intravenously administrated with Ca@H NPs suspension. At different time points (0, 1, 2, 4, 6, 12 and 24 h), the PA images in tumor regions were acquired.

In vivo HIFU Ablation

The 4T1 tumor-bearing mice were irradiated with HIFU (120 W, 5s) under the supervision of diagnostic US imaging 12 h after intravenous injection of Ca@H NPs (10 mg/mL, 200 μL). The grey scale values were compared to the HIFU group (without Ca@H injection). Meanwhile, the tumor tissues were then dissected for H&E staining.

In vivo Combination Therapy

To investigate the efficacy of in vivo HIFU and SDT combination therapy, 4T1 tumor-bearing mice were randomly divided into six groups (n = 5): (1) Control (PBS), (2) SDT, (3) HIFUT, (4) Enhanced HIFUT, (5) Enhanced HIFUT + SDT, and (6) Ca@H Only. Mice in group 1 and group 6 were treated with PBS and Ca@H NPs (10 mg/mL, 200 μL), respectively. Mice in group 3 were irradiated with HIFU (120 W, 5 s). For group 4 and group 5, the tumor regions were irradiated with HIFU (120 W, 5s) at 12 h after intravenous injection of Ca@H NPs (10 mg/mL, 200 μL). After 12 h, for mice in group 2 and 5, SDT was applied by US irradiating the tumor region for 10 min (1.5 W/cm^2). During the therapeutic period, the US irradiation was repeated 3 times (the 1st, 5th, and 10th day). To further evaluate the therapeutic effects, the tumor volumes were measured every three days. The digital photos were collected at 0 d and 15 d. After 15 d, the tumor nodes were excised, weighted, and photographed. The tumor inhibition rates in each group were calculated and compared. Furthermore, the extracted tumor tissues were subjected to H&E and PCNA staining. Proliferation index of PCNA was further analyzed. The brown yellow nucleus (the proliferative cells) was chosen as the positive cells, and proliferation rate was calculated according the equation: Proliferation index (%) = (number of positive cells/number of total cells) × 100%. And the major organs were also stained with H&E.

Biosafety Assessment of Ca@H

For the evaluation of in vivo biosafety, healthy *Kunming* mice (≈20 g, n = 5) were intravenously injected with Ca@H NPs suspension (5 mg/mL or 10 mg/mL, 200 μL). After 30 days of observation, the blood of the mice was collected for hematological analysis, and the major organs were dissected for pathological examination.

Statistical Analyses

The data from each experiment are displayed as the mean ± standard deviation (SD). The statistical analyses were conducted via a Student's *t*-test, $p < 0.05$ is considered as significantly different (*$p < 0.05$, **$p < 0.01$, ***$p < 0.001$).

Results and Discussion

Preparation and Characterisation

Ca@H NPs are synthesized by the gas diffusion method reported previously followed with PEG modification.[34,35] The fabrication procedure is illustrated in Figure 1A. Briefly, HMME and $CaCl_2$ were pre-dissolved in anhydrous ethanol, into which CO_2 from the decomposition of NH_4HCO_3 was slowly diffused. Then, $CaCl_2$ reacted with CO_2 for the growth of $CaCO_3$ NPs, during which HMME was binded and loaded into $CaCO_3$. As demonstrated by SEM (Figure 1B) and TEM (Figure 1C), these as-prepared Ca@H NPs were spherical and uniform, with an average size of about 200 nm. The average hydrodynamic size of Ca@H NPs was determined to be 216.2 ± 46.09 nm as detected by dynamic light scattering (DLS) (Figure 1D). And the surface zeta potential of Ca@H NPs was −22.3 mV (Figure 1E), which showed an enhanced colloidal stability and could potentially inhibit aggregation of these NPs in biological applications.[36,37] The obvious color change from white $CaCO_3$ to brown Ca@H indicated the successful loading of HMME (Figure S1). As shown in Figures 1F and S2A, the UV-Vis spectrum of HMME showed a distinct characteristic band at 398 nm,

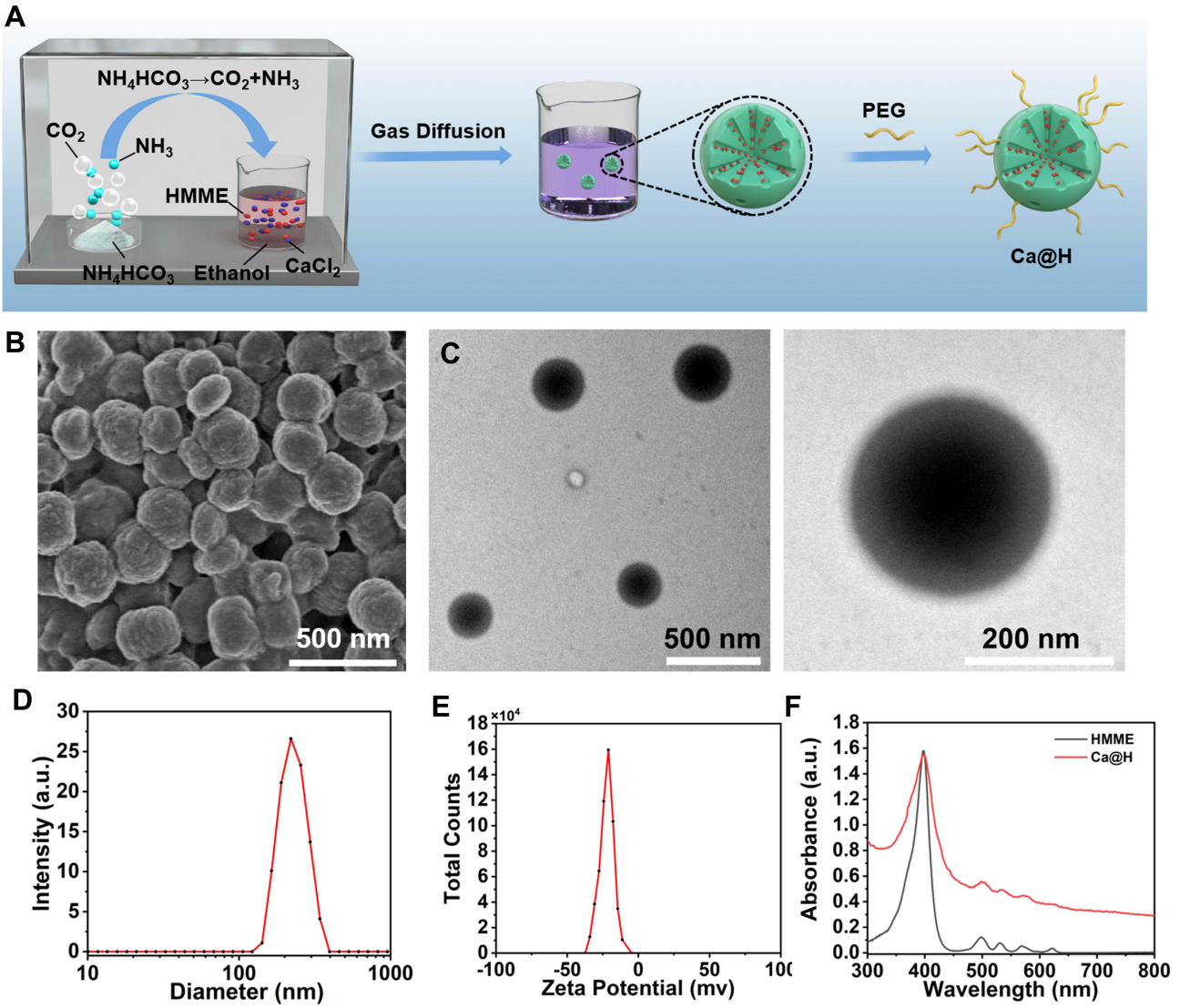

Figure 1 (**A**) Schematic illustration for fabrication of Ca@H NPs. (**B**) SEM and (**C**) TEM images of Ca@H. (**D**) Hydrodynamic diameter of Ca@H NPs detected by DLS. (**E**) Surface zeta potential of Ca@H NPs in aqueous solution. (**F**) UV-Vis spectra of free HMME, and Ca@H suspension.

and fourth weak peaks, which is in accordance with the previous study.[27] The apparent HMME-characteristic absorption peaks of these as-prepared Ca@H NPs further demonstrated the successful loading of HMME. To obtain the loading efficiency of HMME in Ca@H, a standard curve by plotting the absorbance at λ = 398 nm against different HMME concentrations was shown in Figure S2 A and B. The loading efficiency of HMME was calculated to be 89.43 ± 2.97%, indicating the superior capability of $CaCO_3$ in drug loading.

pH-Responsive Performance

$CaCO_3$ is known to be decomposed into Ca^{2+} and CO_2 under acidic conditions (Figure 2A). In order to obtain the acid-responsive behavior of Ca@H NPs, these NPs were dispersed in buffers at pH = 5.5, 6.5 and 7.4, which simulated the microenvironment of lysosomes, tumors, and blood, respectively.[38] An air quality meter was used to quantitatively measure the CO_2 generation (Figure 2B1). As shown in Figure 2B2, a large amount of CO_2 was generated in a concentration- and pH-dependent manner. Furthermore, CO_2 bubbles generated by Ca@H NPs under acidic conditions were also visualized by an optical microscope (Figure 2B2 inset). Moreover, the average diameter changes of Ca@H were monitored under various pH conditions. As shown in Figure 2C, the size of Ca@H NPs appeared relatively stable under neutral condition. In contrast, with prolonged time, the Ca@H NPs showed a time-dependent decrease in sizes at pH 6.5, which facilitated the uptake of NPs by cells.[39–41] Notably, at pH 5.5, these NPs were rapidly disintegrated. It is notable that the pH-responsiveness of Ca@H NPs may be helpful for the subsequent controlled drug release and the prolonged blood circulation under physiological

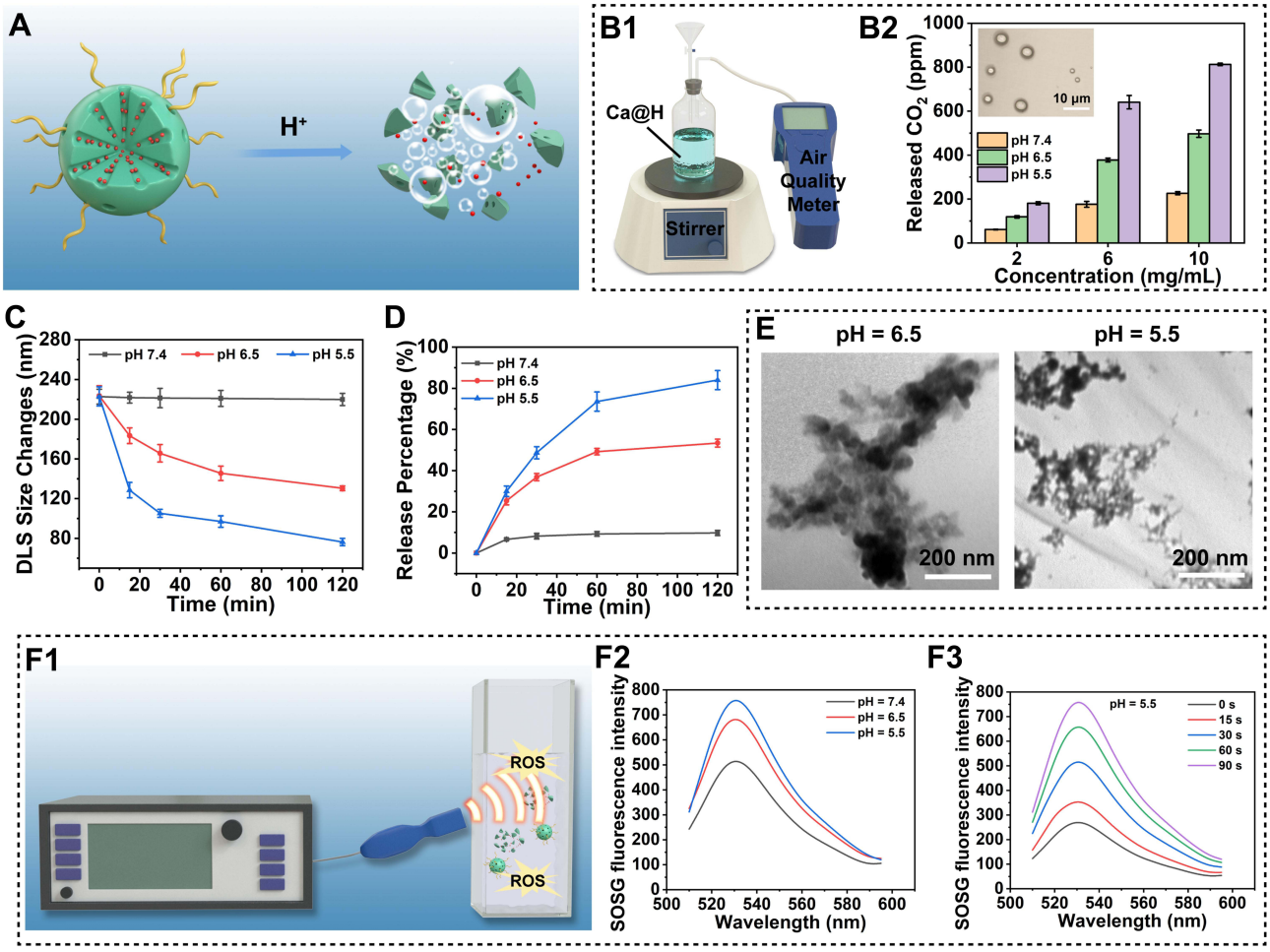

Figure 2 (**A**) Schematic diagram of the pH-activated Ca@H decomposition. (**B1**) Schematic illustration of the quantitative measurement of CO_2 using an air quality meter. (**B2**) CO_2 production diagram of different Ca@H concentrations in buffers at various pH. (**C**) Time-dependent size of Ca@H at different pH values (n = 3). (**D**) The relative released percentage of HMME from Ca@H under various pH (n = 3). (**E**) TEM images of Ca@H in acid buffer (pH = 6.5 or 5.5, stirring for 2 h). (**F1**) Schematic illustration of in vitro ROS generation upon US irradiation. (**F2**) ROS generation of Ca@H at different pH. (**F3**) Time-dependent ROS generation of Ca@H (pH = 5.5).

pH. Then, the release profiles of HMME from Ca@H NPs were quantitatively studied by measuring the absorbance of HMME at 398 nm. It was found that approximately 73.57% of the loaded HMME was released at pH 5.5 after 1 h of reaction, much higher than that of 9.27% at pH 7.4 (Figure 2D), which was consistent with the pH-dependent decomposition results. Morphological changes of Ca@H NPs in acid buffer (pH = 5.5 and 6.5) were further visualized by TEM (Figure 2E). These NPs gradually decomposed and lose their sphere morphology after 2 h under acid conditions. Reasonably, such pH-responsive Ca@H NPs could provide new possibilities for enhanced antitumor efficacy. Considering that the released HMME can be used as a sonosensitizer, SOSG was used to detect the ROS generation upon US irradiation (Figure 2F1). As shown in Figures 2F2, F3 and S3, the ROS generation capability exhibited pH and US irradiation time-dependent features, indicating the potential of Ca@H for SDT. Furthermore, the singlet oxygen yield of Ca@H NPs was measured by monitoring the dye-sensitized photooxidation of DPBF. According to Figure S4, $K^{Ca@H}$ and K^{HMME} were fitted as 0.0013 and 0.0018, respectively. Thus, the singlet oxygen yield of Ca@H was calculated to be 0.36, which indicated the potential of Ca@H for SDT in a solid tumor microenvironmental condition.

Intracellular Uptake of Ca@H and ROS Generation

The effective accumulation of Ca@H NPs in tumor cells is a prerequisite for nanotherapeutics against cancer. Therefore, we evaluated the endocytosis behaviours of Ca@H NPs by 4T1 cells using CLSM and flow cytometry. As depicted in Figure 3A and 3B, red fluorescence originating from HMME was detected in cells after 4 h incubation at pH 6.0 and pH7.4 group, but the fluorescence was much stronger at pH 6.0 group than that of at pH 7.4 group, suggesting the efficient cellular uptake of Ca@H NPs in acidic environment. This phenomenon could be explained by the decreased size of Ca@H NPs under acidic condition, which would promote the endocytosis of cells. While at pH = 7.4, HMME was likely to be confined inside $CaCO_3$ NPs, the fluorescence was blocked by the carrier shell.

The ROS generation at the cellular level was evaluated by a ROS probe, DCFH-DA, which is non-fluorescent but can be oxidized by ROS to generate green-fluorescent dichlorofluorescein (DCF).[42] Both CLSM and flow cytometry were used to investigate the potential of Ca@H NPs to generate ROS in the presence of US irradiation. Upon US irradiation, 4T1 cells presented significant green fluorescence after incubation with Ca@H NPs (pH = 6.0 and 7.4), indicating the excellent ROS generation (Figure 3C). However, the fluorescence intensities of cells at pH 6.0 was stronger than that of pH 7.4, which may be related to a more efficient release of HMME from Ca@H. Cells treated with only US irradiation or only Ca@H NPs at both pH = 7.4 and pH = 6.0 did not show obvious green fluorescence. Fluorescent intensities within three microscopic fields for each group were also quantified using Image J software to confirm the statistical differences (Figure S5). Additionally, the flow cytometry analysis from Figure 3D showed that the relative fluorescence intensity in Ca@H + US (pH = 6.0 and 7.4) was higher than the other groups (Control, US, and Ca@H at both pH = 7.4 and pH = 6.0), and the Ca@H + US (pH = 6.0) group showed the highest fluorescence intensity, which is consistent with CLSM results.

In vitro Cytotoxicity of Ca@H NPs

The cytotoxicity of Ca@H NPs and its combination with US irradiation against 4T1 cells were assessed. In a 96 well-plate, cells were seeded at 1×10^4 per well to allow adhere overnight. The media were then replaced with media with different concentrations of Ca@H NPs for 4 h, 12 h, and 24 h, respectively. Then, a standard CCK-8 assay was performed to detect the cell viabilities. As shown in Figure 4A, in the absence of US irradiation, Ca@H NPs exert no evident toxicity on cells even at HMME concentration of 30 μg/mL. At both pH = 7.4 and pH = 6.0, US only also showed negligible influence. In comparison, the cytotoxicity of Ca@H NPs at both pH = 7.4 and pH = 6.0 presented a concentration-dependent manner when US irradiation was combined (Figure 4B). In the presence of both Ca@H NPs and US, specifically, we observed that the cell viabilities were dramatically decreased at pH = 6.0, lower than that at pH = 7.4, indicating the strong cell-killing effects of Ca@H + US under acid conditions. This therapeutic efficacy was further confirmed by CLSM images after the cells were costained by CAM and PI (Figure 4C). Similarly, most cells were killed (represented by the red fluorescence) after Ca@H+ US (pH = 6.0) treatment. There was a higher percentage of live cells (represented by the green fluorescence) after the treatment of Ca@H + US (pH = 7.4), which may be ascribed to the less efficient release of

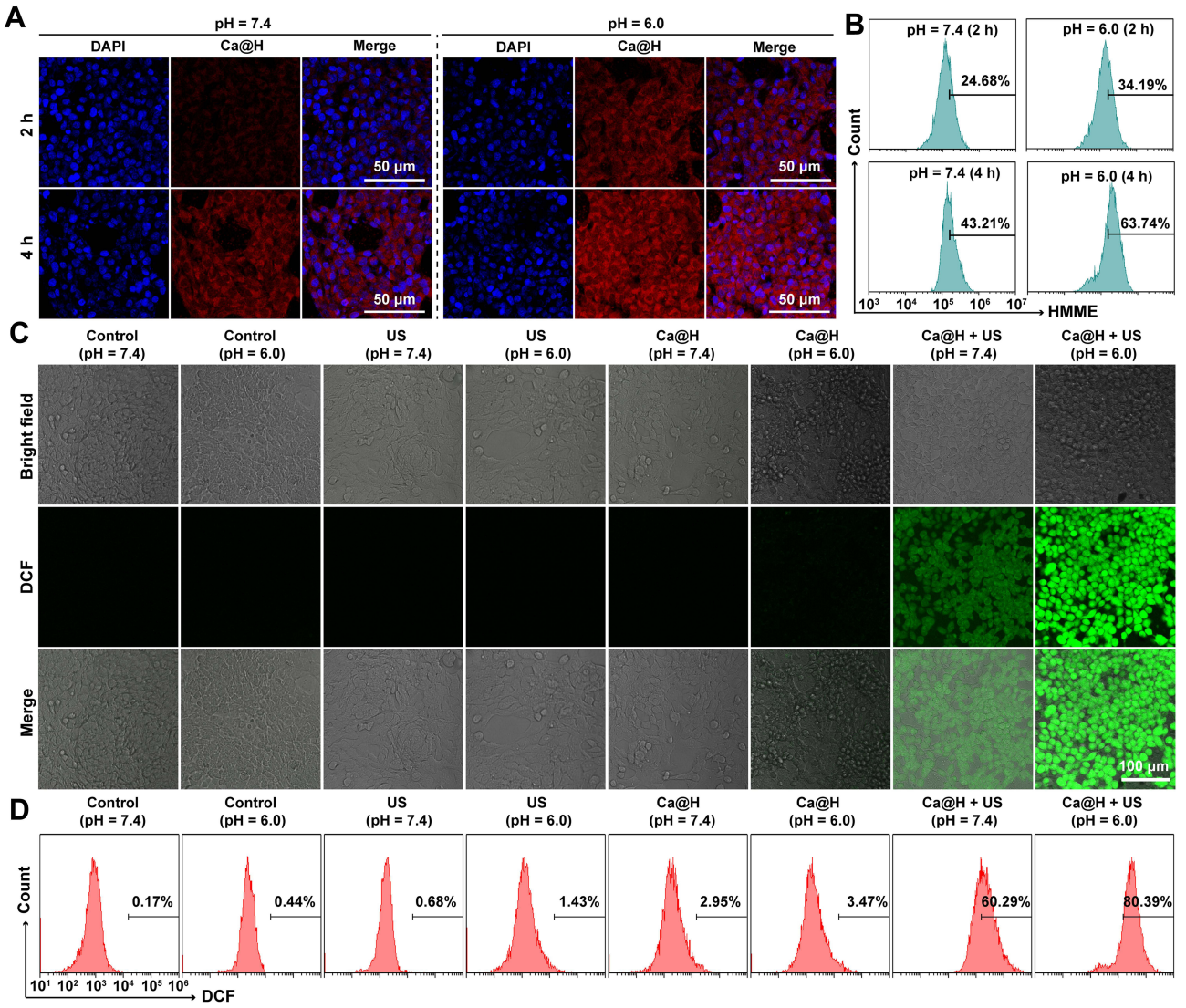

Figure 3 (**A**) CLSM images of 4T1 cells incubated with Ca@H in neutral or acid medium for 2 h and 4 h and (**B**) the correspond relative endocytosis rates of Ca@H analysed by flow cytometry. (**C**) CLSM images of intracellular ROS generation detected by DCFH-DA probe after various treatments. (**D**) Quantitative analysis of ROS generation in 4T1 cells after various treatments.

HMME from $CaCO_3$ under physiological condition. These desirable results demonstrated that Ca@H combined with US can induce highly efficient SDT in vitro, encouraging the following in vivo exploration for antitumor therapy.

Ex vivo Enhanced HIFUT

Studies have reported that microbubbles could enhance the HIFUT via a cavitation effect which is often associated with an enlarged tumor ablation area.[43,44] By virtue of its inherent properties, $CaCO_3$ can be decomposed to produce abundant CO_2 bubbles under acid conditions. Therefore, the enhanced effect of Ca@H on HIFU was studied. Initially, an ex vivo evaluation was performed by using bovine liver as an experimental model after the administration of Ca@H NPs via intro-tissue injection (Figure 5A). The results are shown in Figure 5B, at pH 7.4, the $CaCO_3$ induced a mild change in grayscale after HIFU exposure. However, a notable grayscale change occurred in the Ca@H (pH = 5.5) group, which could be resulted from CO_2 bubbles produced by the decomposition of $CaCO_3$ in the nanocomposite. The quantitative analysis showed that grey value changes at pH = 5.5 or 6.5 group were significantly higher than that at pH = 7.4 (Figure 5C). In addition, the ablation area difference among the three groups was markable in photographic images, showing that the ablated area was the largest under pH 5.5, followed by pH 6.5, and the smallest under

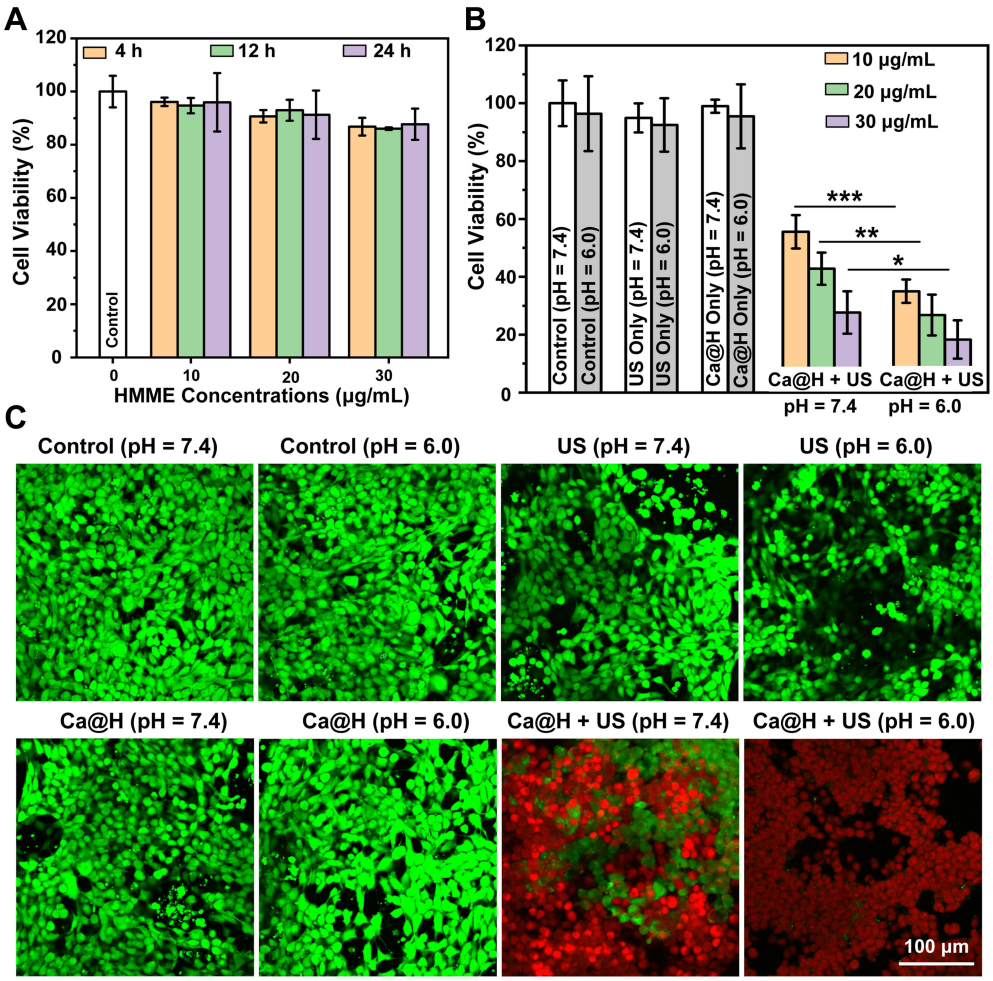

Figure 4 (**A**) Cytotoxicity of Ca@H after incubation with 4T1 cells at different concentrations of Ca@H for 4 h, 12 h and 24 h (n = 5). (**B**) Cell viabilities of 4T1 cells after various treatments (n = 5, *t* test, *p < 0.05, **p < 0.01, ***p < 0.001). (**C**) CLSM images of cells co-stained with CAM and PI after different treatments.

neutral conditions (Figure 5D). The enhanced HIFUT of Ca@H in acid condition was further confirmed by measuring the ablation volume (Figure 5E). Pathological examinations (Figure 5F) revealed that large number of cells were destroyed by HIFU in the presence of Ca@H dispersed in acid buffer, presenting large vacuoles in the sections. These results unanimously indicated that Ca@H NPs could act as synergistic agents for HIFUT especially in the presence of mild acidity. Ultrastructural analysis of liver tissues after different treatments were carried out by TEM. As shown in Figure S6, in the control group, the cell structure remained intact. However, in the HIFU-treated groups, cell nucleus and organelle structures were mostly significantly damaged, and the cell and nuclear membranes were severely ruptured. Besides, cell vacuolization (red arrows) was observed after HIFU irradiation.

PA Imaging Performance of Ca@H

PA imaging is an emerging biomedical imaging technology that can be used for tracking the distribution of nanocarriers at targeted regions.[45–47] After administration, Ca@H NPs could pass through leaky tumor vessels and gathered in tumor tissues by the enhanced permeability and retention (EPR) effect during blood circulation. As indicated by in vitro assessment results, Ca@H NPs would potentially decompose in the acidic tumor microenvironment, and subsequently produce CO_2 and release HMME, the latter has been widely used as a contrast agent for PA imaging. Moreover, it has been reported that CO_2 can absorb certain irradiation energy, thereby increasing the local temperature, and the gas undergoes thermoelastic expansion to produce ultrasonic waves, which are visualized by the acoustic wave detector and displayed as PA signals.[26,29] As showed in Figure 6A and B, in acidic buffers (at pH = 6.5 and 5.5), Ca@H NPs showed strong

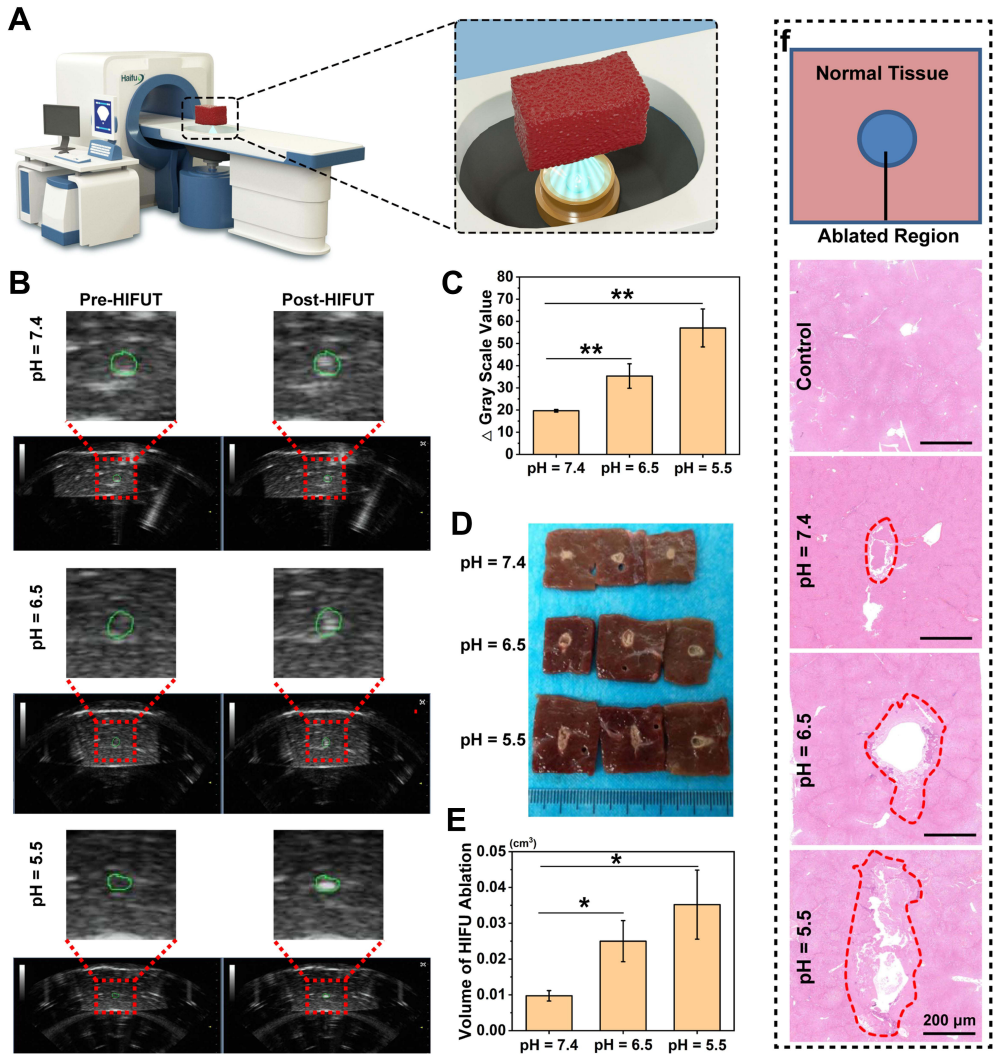

Figure 5 (**A**) Schematic illustration of the ex vivo HIFU ablation. (**B**) Representative US images of bovine liver tissues before and post HIFU ablation (the green circles indicate the areas focused by HIFU). (**C**) Gray scale value changes of bovine liver tissues after HIFU ablation (n = 3, *t* test, **p < 0.01). (**D**) The corresponding digital photos of bovine liver tissues after HIFU ablation. (**E**) Tissue volume changes of HIFU ablation (n = 3, *t* test, *p < 0.05). (**F**) H&E staining of bovine liver tissue after HIFU ablation (the red circles represent the damaged areas after HIFU irradiation).

PA signals. In contrast, almost no PA signal was observed at pH = 7.4 probably because there was almost no CO_2 production and HMME release. $CaCO_3$ NPs without HMME loading presented relatively weak PA signals under acidic conditions. The signals gradually increased initially and then decreased, because the production of CO_2 gradually increased in the early stage and decreased with the volatilization of the gas in the later stage, which was consistent with previous reports.[48,49] When these nanoparticles were intravenously injected into 4T1 tumor-bearing mice, the PA intensity within the tumor region was increased and reached to the peak at 12 h (Figure 6C and D). This imaging was resulted from an effective CO_2 and HMME release in tumor, providing the therapeutic time window for the following in vivo therapy.

In vivo Enhanced HIFUT

4T1 tumor-bearing mice models were established and Ca@H NPs were intravenously injected. After 12 h of the injection, the US imaging-guided HIFUT was carried out (Figure 7A). After HIFU ablation, the targeted zone appeared hyperechoic, and the grayscale value increased significantly (Figure 7B and C). After that, the tumor tissues were stained with H&E for

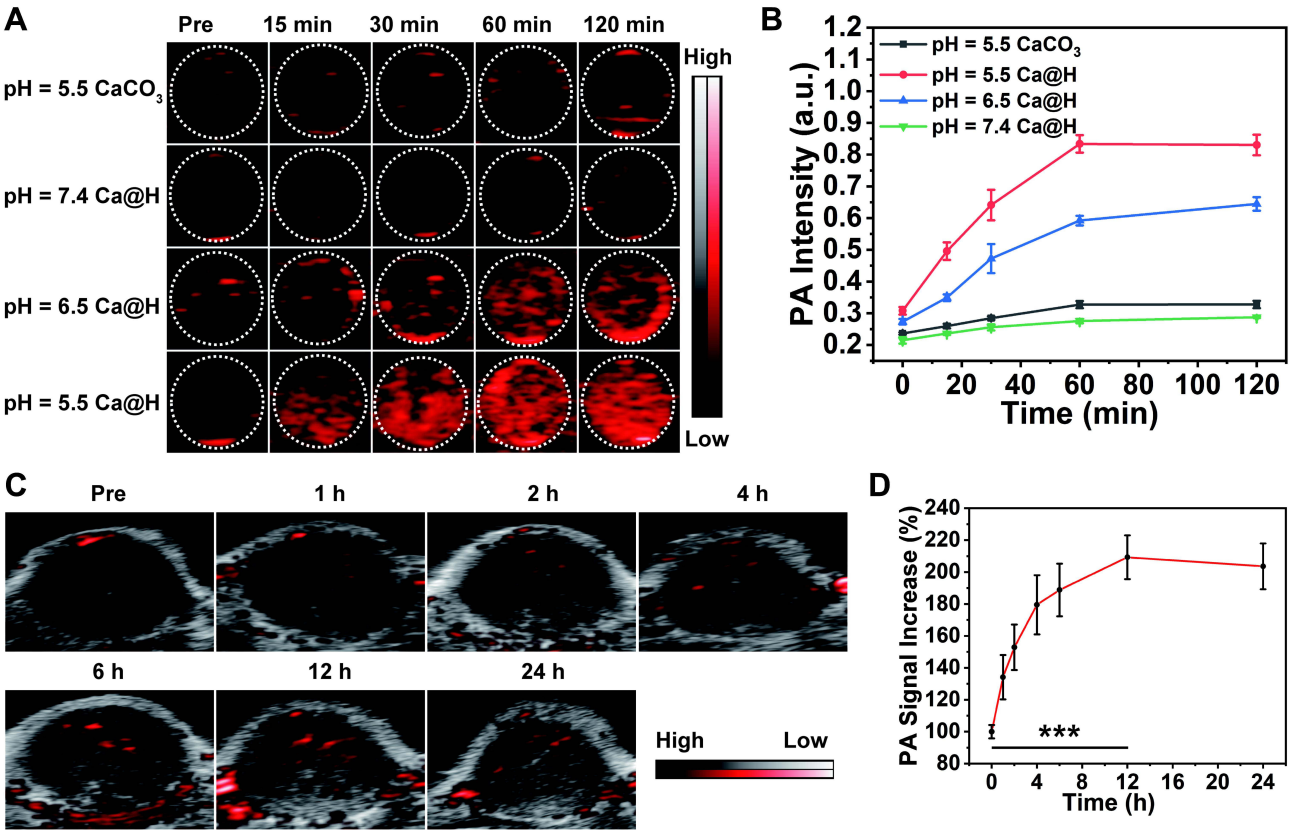

Figure 6 (**A**) In vitro PA images of $CaCO_3$ or Ca@H dispersed in buffers at various pH and (**B**) quantitative analysis of PA signal intensities (n = 3). (**C**) In vivo PA imaging at different time points. (**D**) In vivo PA signal increase (%) compared to pre-injection of Ca@H (n = 5, *t* test, ***p < 0.001).

microscopic examination. As showed in Figure 7D, the cells in the HIFU only group showed a small area of coagulative necrosis/apoptosis. On the contrary, extensive necrosis occurred when the tumor received enhanced HIFUT (receiving Ca@H NPs injection). It can be seen that cells suffered from severe damage with a lot of vacuoles. And there was a sharp demarcation between non-ablated and ablated regions. However, the local HIFUT arises a knotty issue, also known as incomplete ablation. As at the junction of pathological tissue and normal tissue, if HIFU ablation is performed further, normal tissue may be damaged. Compared to HIFUT, SDT is based on US (usually with low energy) and sonosensitizers. This low-energy US usually does not cause damage to the tissue without sonosensitizers. Therefore, we attempted to employ SDT to fight against residual tumor tissues after HIFUT. Therapeutic effects of HIFUT combined with SDT in vivo will be shown in the next section.

HIFUT Combined with SDT Against 4T1 Tumors

In order to eliminate tumor tissues as completely as possible, Ca@H-based SDT was carried out after HIFUT. The experimental design is shown in Figure 8A. With the same setups, repetitive ultrasound irradiation treatments exhibited significantly higher antitumor effects than that of single ultrasound treatment.[50,51] The extended irradiation can also make the most use of sonosensitizers. Many studies also use multiple ultrasound irradiations to implement SDT.[52–54] Therefore, SDT repeated 3 times (the 1st, 5th, and 10th day) in this study. After 12 h of Ca@H NPs administration, mice were subjected to HIFU ablation. As a result, according to Figures 8B, 8C, S7A and S7B, the tumors in groups 1 and 6 grew relatively fast. In contrast, the tumor growth in the Enhanced HIFUT + SDT group was inhibited greatly. After 15 days of treatment, the tumor tissues in each group were dissected and compared. As indicated in digital

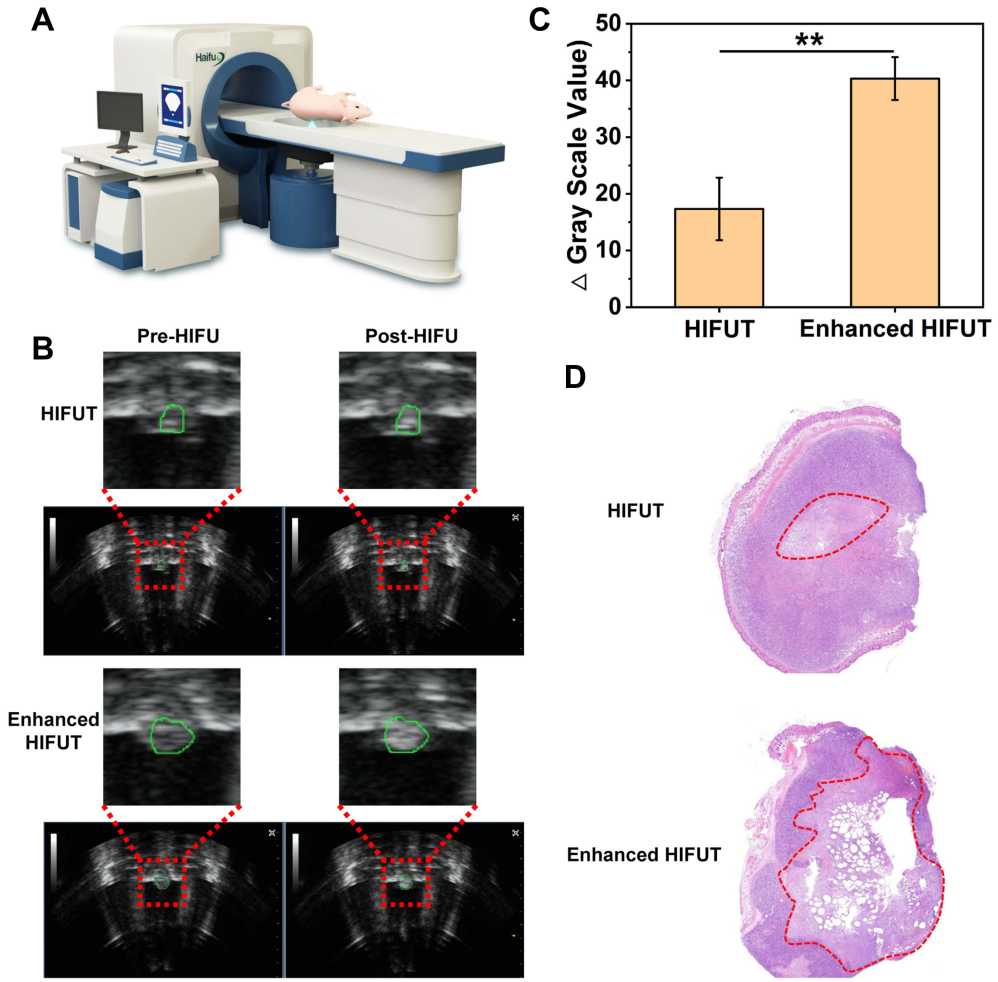

Figure 7 (**A**) Schematic illustration of the in vivo HIFU ablation. (**B**) Representative US images of tumor tissues before or post HIFUT with and without administration of Ca@H (the green circles indicate the areas focused by HIFU). (**C**) Gray scale value changes of tumor tissues after HIFU ablation with and without administration of Ca@H (n = 3, *t* test, **p < 0.01). (**D**) H&E staining of tumor tissues exposed to HIFU with and without administration of Ca@H (the red circles represent the damaged areas after HIFU irradiation).

photographs (Figures 8D and S7C), tumors treated with enhanced HIFUT or enhanced HIFUT + SDT showed the most destruction, which was resulted from the enhanced HIFU ablation. The weight of tumors in the group of enhanced HIFUT + SDT was the lowest (Figures 8E and S7D). The inhibition rate of the combined treatment group is 61.04%, compared with 49.54% for group 4, 37.94% for group 3, 22.54% for group 2, and 6.49% for group 6, respectively (Figures 8F and S7E). During the therapeutic period, there is no detectable weight fluctuation after various treatments (Figures 8G and S7F), demonstrating the satisfactory safety of these treatments. Tumor tissues were sliced for H&E and PCNA staining to further assess the therapeutic effects (Figures 9A and S7G). Compared to the control group, the group treated with enhanced HIFUT + SDT showed the most serious cell damage, whereas the SDT groups displayed mild impairment on tumor cells. Correspondingly, the proliferation index in the enhanced HIFUT + SDT-treated group was the lowest, which exhibited small number of PCNA-positive cells (Figure S8). To examine the potential toxicity to mice after Ca@H-based therapy, the major organs were collected for H&E staining at the end of the treatments (Figures 9B and S7H). The results showed no apparent change was detected in all groups, indicating the high biosafety of these therapeutic modalities.

Desirable therapeutic agents should not only possess outstanding theranostics ability but also exhibit good

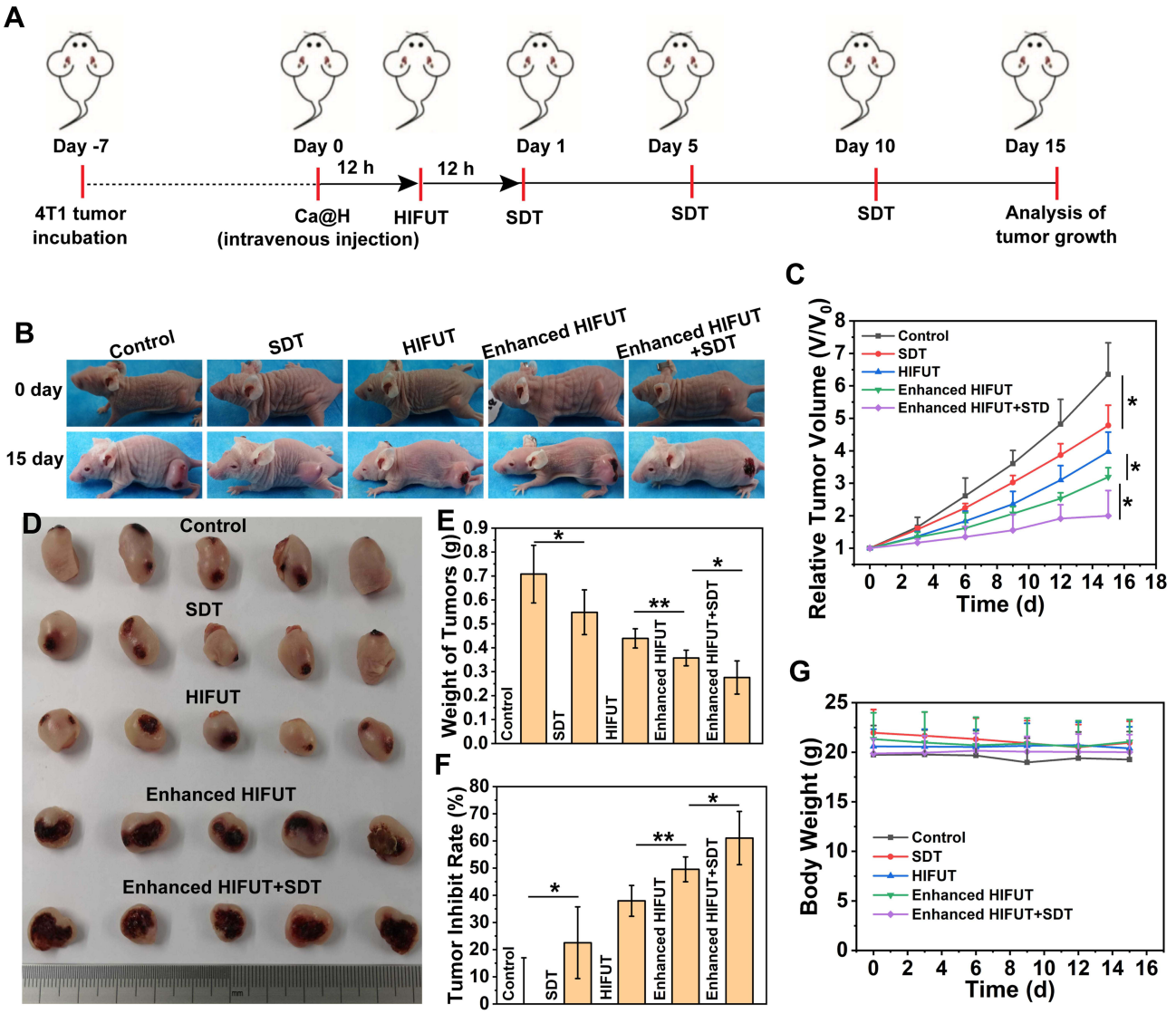

Figure 8 (**A**) Experimental design of the in vivo treatment. (**B**) Digital photos of 4T1 tumor bearing mice before and post various treatments. (**C**) Tumor growth curve of 4T1 tumor-bearing mice after various treatments (n = 5, *t* test, *p < 0.05). (**D**) Digital photo of tumors after various treatments. (**E**) Weight of tumor tissues excised from each group (n = 5, *t* test, *p < 0.05, **p < 0.01). (**F**) Tumor inhibition rates after different treatments (n = 5, *t* test, *p < 0.05, **p < 0.01). (**G**) Body weight of mice during the therapeutic period (n = 5).

biocompatibility. In this regard, the preliminary exploration of mice blood index and tissue change was studied. Ten healthy mice were intravenously injected with various concentrations of Ca@H (n = 5). After 30 days of the injection, the blood and major organs were harvested for systemic examination, and mice with PBS administration were set as the control. It was found that no obvious adverse effects on both blood biochemical criterion and complete blood count (Figure 10A). Similarly, the pathologic tissue slices of major organs showed that no detectable change was observed for various dose (Figure 10B), suggesting the relatively high safety of these Ca@H NPs for further clinic application.

Conclusion

In summary, pH-responsive Ca@H NPs have been successfully constructed for PA imaging-guided/monitored HIFUT combined with SDT. In the tumor microenvironment, these Ca@H NPs gradually decomposed responding to the mild acidity. The produced CO_2 and released HMME could both enhance PA imaging, providing US-based therapeutic guidance and monitoring. The generated CO_2 bubbles enhanced HIFUT via a cavitation effect and could induce an enlarged ablation area, which has been demonstrated both in ex vitro and in vivo. Moderate-intensity long sustaining US-based SDT was further performed for the treatment of residual lesions. The

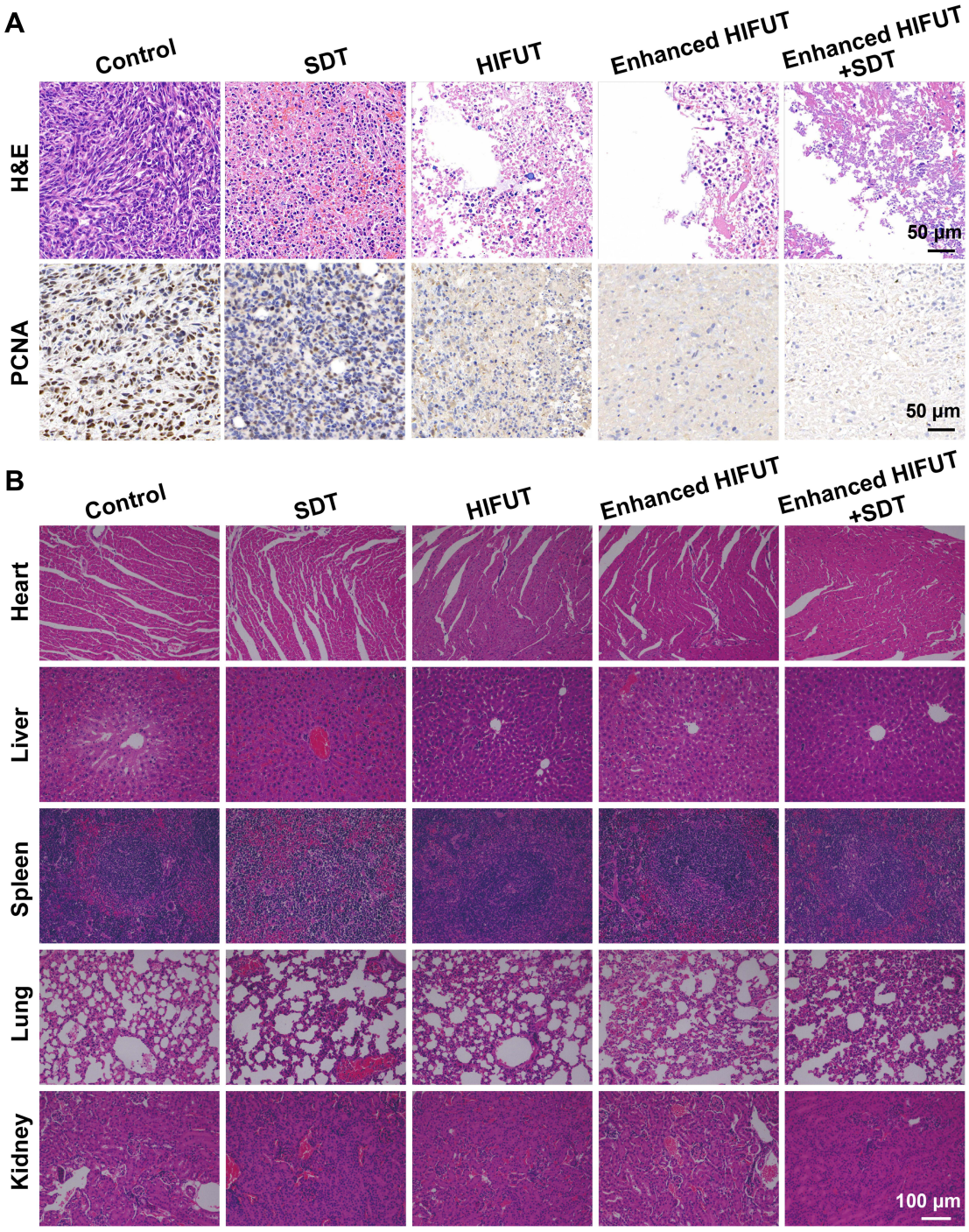

Figure 9 (**A**) H&E and PCNA staining of tumor tissues after various treatments. (**B**) H&E staining of major organs of mice after various treatments.

therapeutic effect of SDT has also been evaluated both in vitro and in vivo. The combination of these two US-based therapies showed highly efficient tumor inhibition. In addition, Ca@H NPs demonstrated high-standard biosafety. With the assistance of pH-responsive Ca@H NPs, it is expected that the combination of HIFUT and SDT can significantly increase the ablation efficacy and treat the residual tumor tissues, which is promising for non-invasive tumor therapy in the future.

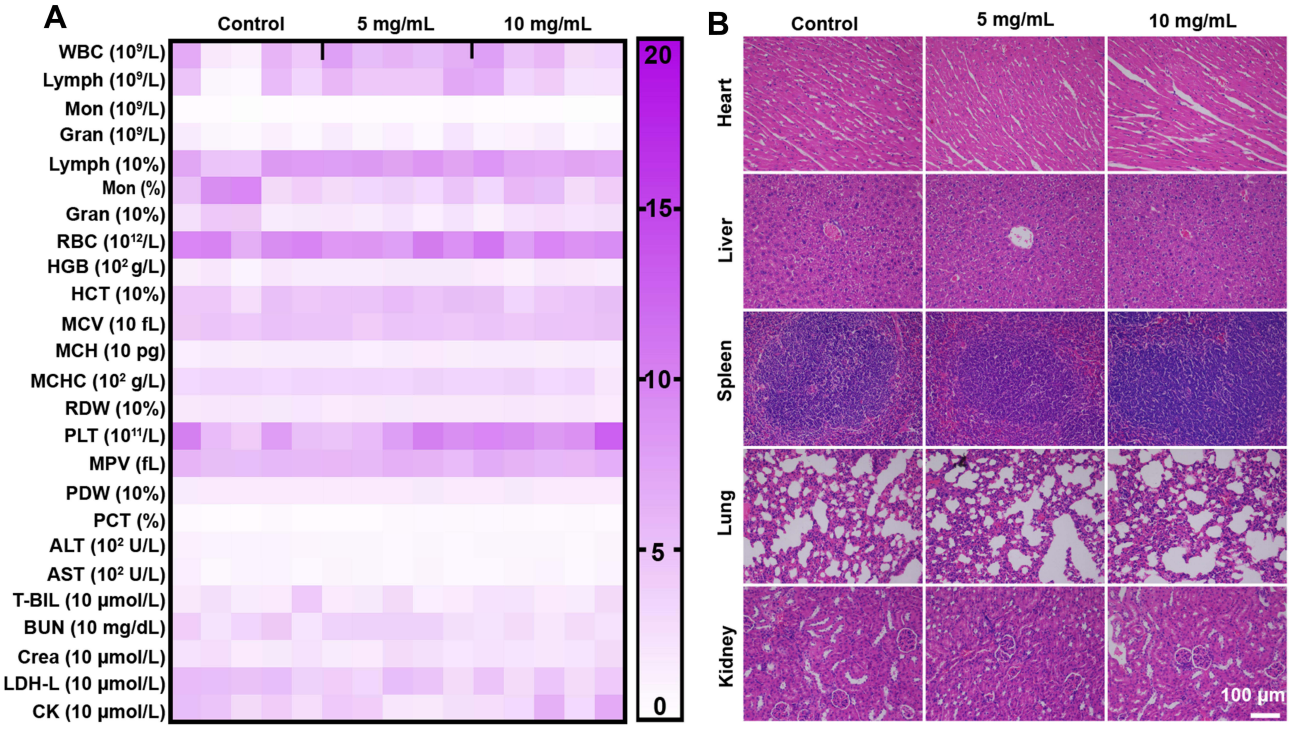

Figure 10 (**A**) Haematological analysis of mice after intravenously injected with Ca@H. (**B**) H&E staining of major organs excised from Ca@H treated-mice.

Acknowledgments

This work was supported by the National Natural Science Foundation of China (82071926, 81630047, 81801711).

Disclosure

There are no conflicts to declare.

References

1. Zhou LQ, Li P, Cui XW, Dietrich CF. Ultrasound nanotheranostics in fighting cancer: advances and prospects. *Cancer Lett*. 2020;470:204–219. doi:10.1016/j.canlet.2019.11.034
2. Tang H, Zheng Y, Chen Y. Materials chemistry of nanoultrasonic biomedicine. *Adv Mater*. 2017;29(10):1604105. doi:10.1002/adma.201604105
3. Martínez-Fernández R, Máñez-Miró JU, Rodríguez-Rojas R, et al. Randomized trial of focused ultrasound subthalamotomy for parkinson's disease. *N Engl J Med*. 2020;383(26):2501–2513. doi:10.1056/NEJMoa2016311
4. Liang S, Liu B, Xiao X, et al. A robust narrow bandgap vanadium tetrasulfide sonosensitizer optimized by charge separation engineering for enhanced sonodynamic cancer therapy. *Adv Mater*. 2021;33(36):2101467. doi:10.1002/adma.202101467
5. Villemain O, Baranger J, Friedberg MK, et al. Ultrafast ultrasound imaging in pediatric and adult cardiology: techniques, applications, and perspectives. *JACC Cardiovasc Imaging*. 2020;13(8):1771–1791. doi:10.1016/j.jcmg.2019.09.019
6. Becciolini M, Pivec C, Riegler G. Ultrasound imaging of the deep peroneal nerve. *J Ultrasound Med*. 2021;40(4):821–838. doi:10.1002/jum.15455
7. Omata D, Unga J, Suzuki R, Maruyama K. Lipid-based microbubbles and ultrasound for therapeutic application. *Adv Drug Deliv Rev*. 2020;154–155:236–244. doi:10.1016/j.addr.2020.07.005
8. Chowdhury SM, Abou-Elkacem L, Lee T, Dahl J, Lutz AM. Ultrasound and microbubble mediated therapeutic delivery: underlying mechanisms and future outlook. *J Control Release*. 2020;326(10):75–90. doi:10.1016/j.jconrel.2020.06.008
9. Son S, Kim JH, Wang X, et al. Multifunctional sonosensitizers in sonodynamic cancer therapy. *Chem Soc Rev*. 2020;49(11):3244–3261. doi:10.1039/c9cs00648f
10. Shah BR, Lehman VT, Kaufmann TJ, et al. Advanced MRI techniques for transcranial high intensity focused ultrasound targeting. *Brain*. 2020;143(9):2664–2672. doi:10.1093/brain/awaa107
11. Cazzato RL, de Rubeis G, de Marini P, et al. Percutaneous microwave ablation of bone tumors: a systematic review. *Eur Radiol*. 2021;31(5):3530–3541. doi:10.1007/s00330-020-07382-8
12. van den Bijgaart RJ, Eikelenboom DC, Hoogenboom M, Fütterer JJ, den Brok MH, Adema GJ. Thermal and mechanical high-intensity focused ultrasound: perspectives on tumor ablation, immune effects and combination strategies. *Cancer Immunol Immunother*. 2017;66(2):247–258. doi:10.1007/s00262-016-1891-9
13. Al-Bataineh O, Jenne J, Huber P. Clinical and future applications of high intensity focused ultrasound in cancer. *Cancer Treat Rev*. 2012;38(5):346–353. doi:10.1016/j.ctrv.2011.08.004
14. Chen Y, Chen H, Shi J. Nanobiotechnology promotes noninvasive high-intensity focused ultrasound cancer surgery. *Adv Healthc Mater*. 2015;4(1):158–165. doi:10.1002/adhm.201400127
15. Loreto BF, Rodney LF, Katsuro T. High-intensity focused ultrasound in the treatment of breast cancer. *Curr Med Chem*. 2020;27:1–10. doi:10.2174/0929867327666201111143206
16. Li Y, Hao L, Liu F, et al. Cell penetrating peptide-modified nanoparticles for tumor targeted imaging and synergistic effect of sonodynamic/HIFU therapy. *Int J Nanomedicine*. 2019;14:5875–5894. doi:10.2147/ijn.S212184

17. Maloney E, Hwang JH. Emerging HIFU applications in cancer therapy. *Int J Hyperthermia*. 2015;31(3):302–309. doi:10.3109/02656736.2014.969789
18. Poissonnier L, Chapelon JY, Rouvière O, et al. Control of prostate cancer by transrectal HIFU in 227 patients. *Eur Urol*. 2007;51(2):381–387. doi:10.1016/j.eururo.2006.04.012
19. Yu L, Hu P, Chen Y. Gas-generating nanoplatforms: material chemistry, multifunctionality, and gas therapy. *Adv Mater*. 2018;30(49):e1801964. doi:10.1002/adma.201801964
20. Qi C, Lin J, Fu LH, Huang P. Calcium-based biomaterials for diagnosis, treatment, and theranostics. *Chem Soc Rev*. 2018;47(2):357–403. doi:10.1039/c6cs00746e
21. Dong Z, Hao Y, Li Q, et al. Metal-polyphenol-network coated CaCO3 as pH-responsive nanocarriers to enable effective intratumoral penetration and reversal of multidrug resistance for augmented cancer treatments. *Nano Res*. 2020;13(11):3057–3067. doi:10.1007/s12274-020-2972-9
22. Ferreira AM, Vikulina AS, Volodkin D. CaCO(3)crystals as versatile carriers for controlled delivery of antimicrobials. *J Control Release*. 2020;328:470–489. doi:10.1016/j.jconrel.2020.08.061
23. Dong Z, Feng L, Hao Y, et al. Synthesis of hollow biomineralized CaCO(3)-polydopamine nanoparticles for multimodal imaging-guided cancer photodynamic therapy with reduced skin photosensitivity. *J Am Chem Soc*. 2018;140(6):2165–2178. doi:10.1021/jacs.7b11036
24. Dong Z, Feng L, Hao Y, et al. Synthesis of $CaCO_3$-based nanomedicine for enhanced sonodynamic therapy via amplification of tumor oxidative stress. *Chem*. 2020;6(6):1391–1407. doi:10.1016/j.chempr.2020.02.020
25. Qian X, Zheng Y, Chen Y. Micro/Nanoparticle-augmented sonodynamic therapy (SDT): breaking the depth shallow of photoactivation. *Adv Mater*. 2016;28(37):8097–8129. doi:10.1002/adma.201602012
26. Jung E, Kang C, Lee J, et al. Molecularly engineered theranostic nanoparticles for thrombosed vessels: H_2O_2-activatable contrast-enhanced photoacoustic imaging and antithrombotic therapy. *ACS Nano*. 2018;12(1):392–401. doi:10.1021/acsnano.7b06560
27. Yang C, Zhang Y, Luo Y, et al. Dual ultrasound-activatable nanodroplets for highly-penetrative and efficient ovarian cancer theranostics. *J Mater Chem B*. 2020;8(3):380–390. doi:10.1039/c9tb02198a
28. Zhang R, Zhang L, Ran H, et al. A mitochondria-targeted anticancer nanoplatform with deep penetration for enhanced synergistic sonodynamic and starvation therapy. *Biomater Sci*. 2020;8(16):4581–4594. doi:10.1039/d0bm00408a
29. Xu C, Wang Y, Wang E, et al. Effective eradication of tumors by enhancing photoacoustic-imaging-guided combined photothermal therapy and ultrasonic therapy. *Adv Funct Mater*. 2021;31(10):2009314. doi:10.1002/adfm.202009314
30. Cao J, Qiao B, Luo Y, et al. A multimodal imaging-guided nanoreactor for cooperative combination of tumor starvation and multiple mechanism-enhanced mild temperature phototherapy. *Biomater Sci*. 2020;8(23):6561–6578. doi:10.1039/d0bm01350a
31. Adarsh N, Avirah RR, Ramaiah D. Tuning photosensitized singlet oxygen generation efficiency of novel aza-BODIPY dyes. *Org Lett*. 2010;12(24):5720–5723. doi:10.1021/ol102562k
32. He H, Ji S, He Y, et al. Photoconversion-tunable fluorophore vesicles for wavelength-dependent photoinduced cancer therapy. *Adv Mater*. 2017;29(19):1606690. doi:10.1002/adma.201606690
33. Redmond RW, Gamlin JN. A compilation of singlet oxygen yields from biologically relevant molecules. *Photochem Photobiol*. 1999;70(4):391–475. doi:10.1111/j.1751-1097.1999.tb08240.x
34. Dong Z, Feng L, Zhu W, et al. $CaCO_3$ nanoparticles as an ultra-sensitive tumor-pH-responsive nanoplatform enabling real-time drug release monitoring and cancer combination therapy. *Biomaterials*. 2016;110:60–70. doi:10.1016/j.biomaterials.2016.09.025
35. Zhao Y, Lin LN, Lu Y, Chen SF, Dong L, Yu SH. Templating synthesis of preloaded doxorubicin in hollow mesoporous silica nanospheres for biomedical applications. *Adv Mater*. 2010;22(46):5255–5259. doi:10.1002/adma.201002395
36. Karemore MN, Avari JG. Zeta potential as a novel diagnostic tool for preeclampsia. *Pregnancy Hypertens*. 2018;13:187–197. doi:10.1016/j.preghy.2018.06.014
37. Sun Y, Deac A, Zhang GGZ. Assessing physical stability of colloidal dispersions using a turbiscan optical analyzer. *Mol Pharm*. 2019;16(2):877–885. doi:10.1021/acs.molpharmaceut.8b01194
38. Wang Y, Zhou K, Huang G, et al. A nanoparticle-based strategy for the imaging of a broad range of tumours by nonlinear amplification of microenvironment signals. *Nat Mater*. 2014;13(2):204–212. doi:10.1038/nmat3819
39. Chauhan VP, Stylianopoulos T, Martin JD, et al. Normalization of tumour blood vessels improves the delivery of nanomedicines in a size-dependent manner. *Nat Nanotechnol*. 2012;7(6):383–388. doi:10.1038/nnano.2012.45
40. Wang C, Chen S, Wang Y, et al. Lipase-triggered water-responsive "pandora's box" for cancer therapy: toward induced neighboring effect and enhanced drug penetration. *Adv Mater*. 2018;30(14):e1706407. doi:10.1002/adma.201706407
41. Salzano G, Costa DF, Sarisozen C, et al. Mixed nanosized polymeric micelles as promoter of doxorubicin and miRNA-34a co-delivery triggered by dual stimuli in tumor tissue. *Small*. 2016;12(35):4837–4848. doi:10.1002/smll.201600925
42. Zhang W, Hu X, Shen Q, Xing D. Mitochondria-specific drug release and reactive oxygen species burst induced by polyprodrug nanoreactors can enhance chemotherapy. *Nat Commun*. 2019;10(1):1704. doi:10.1038/s41467-019-09566-3
43. Blum NT, Yildirim A, Chattaraj R, Goodwin AP. Nanoparticles formed by acoustic destruction of microbubbles and their utilization for imaging and effects on therapy by high intensity focused ultrasound. *Theranostics*. 2017;7(3):694–702. doi:10.7150/thno.17522
44. Huang L, Zhou K, Zhang J, et al. Efficacy and safety of high-intensity focused ultrasound ablation for hepatocellular carcinoma by changing the acoustic environment: microbubble contrast agent (SonoVue) and transcatheter arterial chemoembolization. *Int J Hyperthermia*. 2019;36(1):244–252. doi:10.1080/02656736.2018.1558290
45. Liu Y, Bhattarai P, Dai Z, Chen X. Photothermal therapy and photoacoustic imaging via nanotheranostics in fighting cancer. *Chem Soc Rev*. 2019;48(7):2053–2108. doi:10.1039/c8cs00618k
46. Zhen X, Pu K, Jiang X. Photoacoustic imaging and photothermal therapy of semiconducting polymer nanoparticles: signal amplification and second near-infrared construction. *Small*. 2021;17(6):e2004723. doi:10.1002/smll.202004723
47. Moore C, Jokerst JV. Strategies for image-guided therapy, surgery, and drug delivery using photoacoustic imaging. *Theranostics*. 2019;9(6):1550–1571. doi:10.7150/thno.32362
48. Tan M, Liu W, Liu F, et al. Silk Fibroin-coated nanoagents for acidic lysosome targeting by a functional preservation strategy in cancer chemotherapy. *Theranostics*. 2019;9(4):961–973. doi:10.7150/thno.30765
49. Min KH, Min HS, Lee HJ, et al. pH-controlled gas-generating mineralized nanoparticles: a theranostic agent for ultrasound imaging and therapy of cancers. *ACS Nano*. 2015;9(1):134–145. doi:10.1021/nn506210a
50. Xiong W, Wang P, Hu J, et al. A new sensitizer DVDMS combined with multiple focused ultrasound treatments: an effective antitumor strategy. *Sci Rep*. 2015;5(1):17485. doi:10.1038/srep17485
51. An J, Hu Y-G, Li C, et al. A pH/Ultrasound dual-response biomimetic nanoplatform for nitric oxide gas-sonodynamic combined therapy and repeated ultrasound for relieving hypoxia. *Biomaterials*. 2020;230:119636. doi:10.1016/j.biomaterials.2019.119636

52. Zeng Q, Qiao L, Cheng L, et al. Perfluorohexane-loaded polymeric nanovesicles with oxygen supply for enhanced sonodynamic therapy. *ACS Biomater Sci Eng*. 2020;6(5):2956–2969. doi:10.1021/acsbiomaterials.0c00407
53. Huang P, Qian X, Chen Y, et al. Metalloporphyrin-encapsulated biodegradable nanosystems for highly efficient magnetic resonance imaging-guided sonodynamic cancer therapy. *J Am Chem Soc*. 2017;139(3):1275–1284. doi:10.1021/jacs.6b11846
54. Zeng W, Xu Y, Yang W, Liu K, Bian K, Zhang B. An ultrasound-excitable aggregation-induced emission dye for enhanced sonodynamic therapy of tumors. *Adv Healthc Mater*. 2020;9(17):2000560. doi:10.1002/adhm.202000560